

Communication

# Towards a Large-Area Freestanding Single-Crystal Ferroelectric BaTiO<sub>3</sub> Membrane

Qixiang Wang <sup>1,2</sup> , Hong Fang <sup>1,2</sup>, Di Wang <sup>3</sup>, Jie Wang <sup>1,2</sup>, Nana Zhang <sup>3</sup>, Bin He <sup>3</sup> and Weiming Lü <sup>1,2,3,\*</sup>

<sup>1</sup> Condensed Matter Science and Technology Institute, School of Instrumentation Science and Engineering, Harbin Institute of Technology, Harbin 150080, China; qixiang\_wang@foxmail.com (Q.W.); fanghong.stu@foxmail.com (H.F.); wangjie2647@163.com (J.W.)

<sup>2</sup> Key Lab of Ultra-Precision Intelligent Instrumentation, Ministry of Industry and Information Technology, Harbin Institute of Technology, Harbin 150080, China

<sup>3</sup> Spintronics Institute, School of Physics and Technology, University of Jinan, Jinan 250022, China; wangdi@mail.ujn.edu.cn (D.W.); zhangnana@mail.ujn.edu.cn (N.Z.); sdy\_heb@ujn.edu.cn (B.H.)

\* Correspondence: weiminglv@hit.edu.cn

Received: 16 July 2020; Accepted: 17 August 2020; Published: 21 August 2020



**Abstract:** The fabrication and transfer of freestanding single-crystal ferroelectric membranes deserve intensive investigations as to their potential applications in flexible wearable devices, such as flexible data storage devices and varied sensors in E-skin configurations. In this report, we have shown a comprehensive study approach to the acquisition of a large-area freestanding single-crystal ferroelectric BaTiO<sub>3</sub> by the Sr<sub>3</sub>Al<sub>2</sub>O<sub>6</sub> scarification layer method. By controlling the thickness of the BaTiO<sub>3</sub> and Sr<sub>3</sub>Al<sub>2</sub>O<sub>6</sub>, the exposed area of the Sr<sub>3</sub>Al<sub>2</sub>O<sub>6</sub> interlayer, and the utilization of an additional electrode La<sub>2/3</sub>Sr<sub>1/3</sub>MnO<sub>3</sub> layer, the crack density on the freestanding BaTiO<sub>3</sub> can be dramatically decreased from 24.53% to almost none; then, a more than 700 × 530 μm<sup>2</sup> area high-quality freestanding BaTiO<sub>3</sub> membrane can be achieved. Our results offer a clear and repeatable technology routine for the acquisition of a flexible large-area ferroelectric membrane, which should be instructive to other transition metal oxides as well. Our study can confidently boost flexible device fabrication based on single-crystal transition metal oxides.

**Keywords:** crack density; ferroelectrics; freestanding; single crystal

## 1. Introduction

Flexible single-crystal oxide membranes have attracted tremendous investigations, both experimentally and theoretically, due to their potential applications in wearable devices as well as for aiding our fundamental understanding of flexible electronics [1–3]. Different from the conventional metal [4,5] and organic materials [6,7], which offer a convenient fabrication of flexible membranes, the achievement of flexible transition metal oxides seems a tough task owing to that they always exhibit the nature of rigidity with poor fracture toughness, although transition metal oxides provide the unique physics properties, such as ferroelectricity [8], colossal magnetoresistance [9], and superconductivity [10], etc., benefiting to the multiple functionalities of future flexible wearable devices.

Barium titanate, BaTiO<sub>3</sub> (BTO), one of the most significant lead-free ferroelectrics [11,12], can be integrated in ultrathin all-oxide devices with high quality, such as the ferroelectric tunnel junction [13–15]. Its spontaneous polarization enables us to control the electrostatic state of a device easily by external electric voltage [16,17]. However, it is well known that the pronounced ferroelectricity needs a long-range lattice ordering [18]; thus, the fabrication of a large-area BTO single-crystal flexible membrane without cracks and a non-damage transfer process are definitely crucial.

Aiming for a flexible ferroelectric membrane, recently the ferroelectric BTO-based Van der Waals heterostructure [19] and the scarification layer method [13,20] have been developed rapidly. Although the flexible BTO can be achieved via depositing it on a mica substrate, the Van der Waals heterostructure cannot give a freestanding BTO layer, which blocks the possibility of the transfer process to any desired substrate.

On the other hand, the scarification layer method enables us to get a freestanding ferroelectric layer by the water-solved  $\text{Sr}_3\text{Al}_2\text{O}_6$  (SAO) interlayer [21–24]. It is found that the freestanding single-crystal manganite  $\text{La}_{0.7}\text{Sr}_{0.3}\text{MnO}_3$  [21], superconductor  $\text{YBa}_2\text{Cu}_3\text{O}_{7-x}$  [22], and multiferroic  $\text{BiFeO}_3$  [23] can be lifted off successfully. However, a systematic study on the preparation of a large-area single-crystal membrane without the local crack has not been reported in detail yet. Here, we report on a systemic investigation on the achievement of a large-area without any noticeable cracks. A freestanding ferroelectric BTO film with dimensions larger than  $700 \times 530 \mu\text{m}^2$  has been achieved by the scarification layer method.

## 2. Materials and Methods

The  $\text{Sr}_3\text{Al}_2\text{O}_6$  (SAO) target was prepared by the conventional solid-state method using  $\text{SrCO}_3$  (99.95 purity) and  $\text{Al}_2\text{O}_3$  (99.99 purity) powders (Aladdin Industrial Corporation in China) as the raw materials. The mixed powder was ground by an agate mortar for 8 h and then calcined at  $1150^\circ\text{C}$  for 5 h. After regrinding for 5 h, the powders were pressed into a pallet with a diameter of 30 mm and a thickness of 3.0 mm. Finally, the pallet was sintered in an alumina crucible at  $1250^\circ\text{C}$  for 24 h in air. The  $\text{La}_{2/3}\text{Sr}_{1/3}\text{MnO}_3$  (LSMO) target was mixed by  $\text{SrCO}_3$  (99.95 purity),  $\text{La}_2\text{O}_3$  (99.999 purity), and  $\text{MnO}_2$  (99.95 purity) powders (Aladdin Industrial Corporation in China), and prepared in the same preparation process. The BTO target was the commercial one from the Kurt J. Lesker Company in America.

These targets were used to fabricate the BTO/SAO/STO (001) and LSMO/BTO/SAO/STO (001) heterostructures through a pulsed laser deposition (PLD) system with a KrF excimer laser of 248 nm wavelength. The base pressure was below  $3 \times 10^{-7}$  Torr. During the deposition, the energy of the laser beam was adjusted to be 4.4 and  $6.7 \text{ J/cm}^2$  for the SAO and BTO, while the oxygen partial pressure was maintained at  $5 \times 10^{-5}$  and  $4 \times 10^{-2}$  Torr. The laser pulse frequency was 2 Hz, and the substrate temperature was held at  $700^\circ\text{C}$  and  $750^\circ\text{C}$  for the SAO and BTO, respectively. The LSMO cover layer was grown at  $750^\circ\text{C}$ , using  $6.7 \text{ J/cm}^2$  at 2 Hz in a 0.2 Torr  $\text{O}_2$  atmosphere. The thickness of the membranes was determined by the oscillation intensity of the reflection high-energy electron diffraction (RHEED).

The PFM characterizations were performed using a Dual AC Resonance Tracking piezoresponse force microscope (MFP-3D, Asylum Research, Oxford Instruments, America). The morphology of the membranes was observed by an optical microscope (Leica DM2700M, Leica, Germany).

Approximately 0.5-mm-thick polydimethylsiloxane (PDMS) was spread on a clean silicon wafer to make a flat PDMS sheet. Next, the top surface of the as-grown heterostructure adhered onto the PDMS surface. For obtaining the freestanding BTO membrane, the PDMS/BTO/SAO/STO (001) sample was immersed into de-ionized water for hours to completely dissolve the soluble SAO layer, and the growth substrate to be removed. The freestanding LSMO/BTO heterostructure was obtained in the same manner.

## 3. Results and Discussion

### 3.1. PFM Phase Analysis and Freestanding Membrane Transfer Process

In Figure 1a, we have shown the piezoelectric force microscopy (PFM) image of the BTO on Nb-doped STO to demonstrate that our BTO has an electric field, a switchable ferroelectric nature. The PFM phase image presents the regions with clear contrast, corresponding to the downward and upward polarizations written by  $\pm 5 \text{ V}$ . Thus, we carried out the sacrificial layer method on a BTO layer with the same growth conditions. As shown in Figure 1b, firstly the  $\text{Sr}_3\text{Al}_2\text{O}_6$  sacrificial layer

was deposited onto the SrTiO<sub>3</sub> (001) single-crystal substrate. Secondly, the BTO layer was grown on the SAO layer. Next, the heterostructure was adhered to the PDMS support layer and transferred to deionized water at room temperature for hours. Then the SAO sacrificial layer was dissolved in deionized water and the freestanding BTO membrane was obtained. Finally, we characterized the crack condition of the obtained freestanding BTO membrane by optical microscopy.

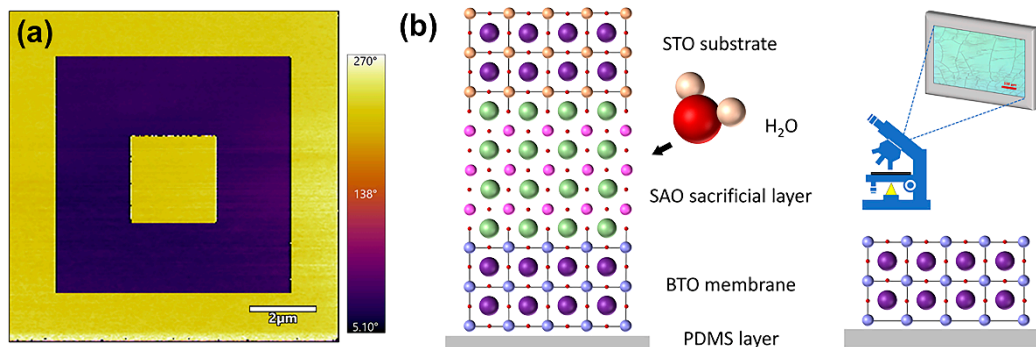


**Figure 1.** (a) The out-of-plane PFM phase image of the BTO membrane grown on an Nb:STO (001) substrate. (b) A schematic of the freestanding membrane transfer process.

### 3.2. The Relationship between Crack Density and Thickness for BTO Membranes

Crack density ( $\rho$ ) is the key parameter to estimate the quality of membranes [25,26].  $\rho$  is determined by the following method: we selected six representative regions from one micrograph to calculate the average crack density. Cracks could be identified from the membrane accurately by setting the micrograph brightness threshold with a code developed in Python. The number of pixel points in the selected region is recorded as the film area ( $S_0$ ), and the number of cracks pixel points, corresponding to the selected region, is recorded as the crack area ( $S_C$ ). The average density of the cracks ( $\rho$ ) can be calculated as  $S_C/S_0 \times 100\%$ . Figure 2e shows the original image of one representative region in Figure 2a, which is enclosed by the red dotted line. The output image is correspondingly shown in Figure 2e. Figure 2a–d shows the surface morphology of the different thickness of the BTO films (8.33, 16.7, 33.3, and 66.7 nm) transferred by a fixed 12.5-nm-thick SAO. Obviously, with the increase in the BTO membrane thickness, the crack density decreases from 19.42% to 9.35% (Figure 2e). From the literature, we know the oxide undergoes a lattice strain release after the flexibility process; thus, this will cause a huge internal strain distribution difference [22]. According to previous studies, similar to the semiconductor and metallic epitaxial layers, ferroelectric oxides are known to relieve the strain as the film thickness is increased [27,28]. Therefore, a large strain gradient is formed in the thinner BTO membrane, resulting in the appearance of dense cracks [29]. Moreover, regular wrinkles can be observed between the cracks (Figure 2a), which are formed perpendicular to the cracks, indicating that the BTO membranes prepared by the PLD system are very uniform [30].

### 3.3. The Relationship between Crack Density and Thickness for SAO Sacrificial Layers

Mechanical flexibility is a key property for flexible memories, yet most oxide single crystals or ceramics are hard and brittle that can be break at  $>4\%$  strain [3]; thus, it is a big challenge for the oxide ferroelectric films to be used in the emerging flexible electronic devices. The strain  $S$  induced on the surface of a substrate by bending the substrate into a radius of  $R$  is given by the simplified equation:  $S = (t_L + t_S)/2R$ , where  $t_L$  is the thickness of the layer and  $t_S$  is the thickness of the substrate [31]. It can be seen from the simplified equation that the thinner film has excellent mechanical flexibility. So preparing high-quality 8.33-nm-thick BTO membranes should be a purpose for further exploration. Figure 3a–c present the evolution of cracks in the 8.33-nm-thick BTO membranes, which separated from the different thickness of the SAO sacrificial layers. It is clear that  $\rho$  decreases from 24.53% to almost none with decreasing of the SAO layer thickness (Figure 3d). The thinner SAO sacrificial layer makes

the dissolved procedure much slower [21], and the stress between the membrane and the substrate gradually disappears, maintaining the integrity of the BTO membrane. When the SAO sacrificial layer thickness decreases down to 6.25 nm, the dissolution time is up to 24 h, and then no cracks appear in the partial areas.

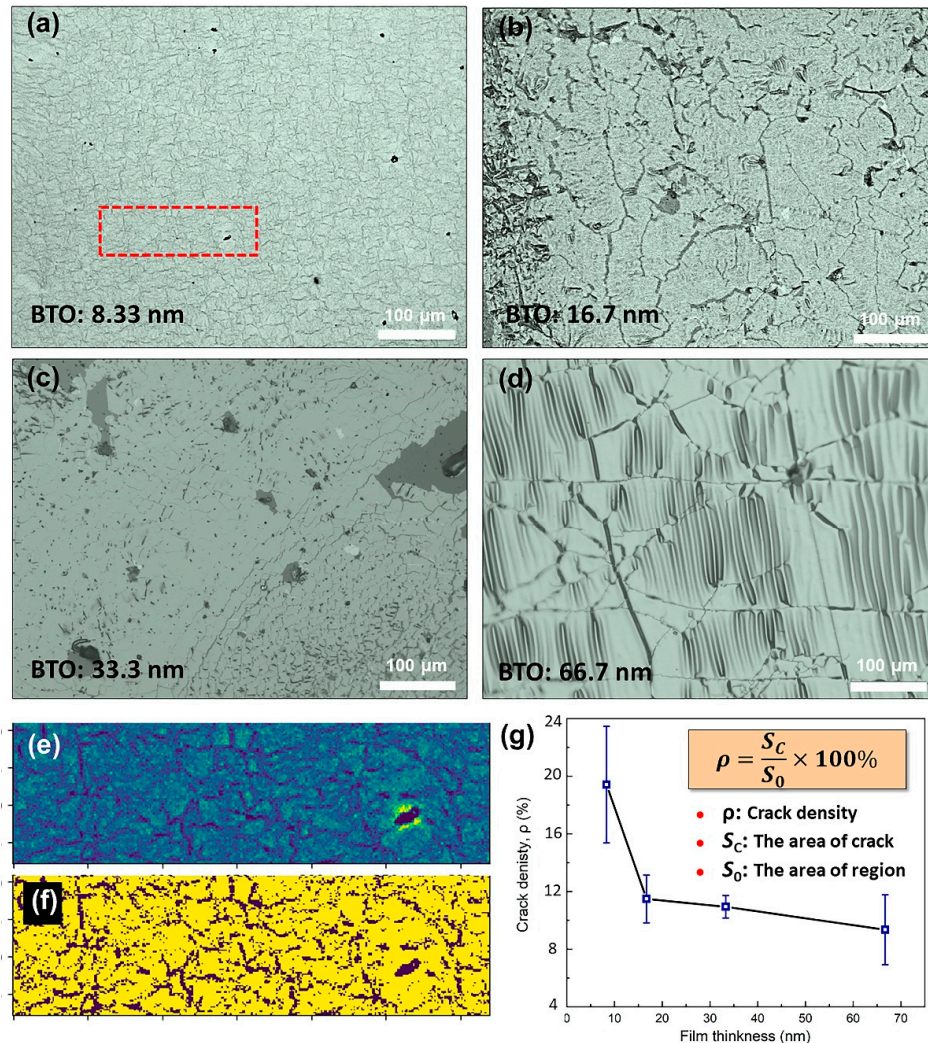


**Figure 2.** Optical micrographs of the BTO membranes with different thickness. (a) 8.33 nm; (b) 16.7 nm; (c) 33.3 nm; (d) 66.7 nm. (e) Original image of the representative region in Figure 2a, which is enclosed by the red dotted line. (f) The output image corresponding to Figure 2e. (g) Variation in the crack density for the BTO membranes.

### 3.4. Process Improvement for High-Quality Membranes

Figure 3a,e show the two samples with the same preparation process, but the transfer processes between them are slightly different. Despite the large aspect ratio ( $700 \times 530 \mu\text{m}^2$ ), almost no cracks were observed on the freestanding BTO membrane across the entire surface as a result of the improved transfer process, as shown in Figure 3a. On the other hand, Figure 3e presents the optical morphology of the BTO membrane, which was taken out from the deionized water directly, and lots of irregular and wide cracks on the surface can be seen clearly. This phenomenon is likely to be caused by water surface tension, which tears the ultrathin membrane when it separated from the substrate. To avoid the influence of water surface tension, the whole structure, including the substrate, was smoothly transferred to ethanol for 5 s, and then heated at 40 °C for 1 min to evaporate the water and alcohol. By this method, a large-area high-quality freestanding BTO membrane can be achieved.

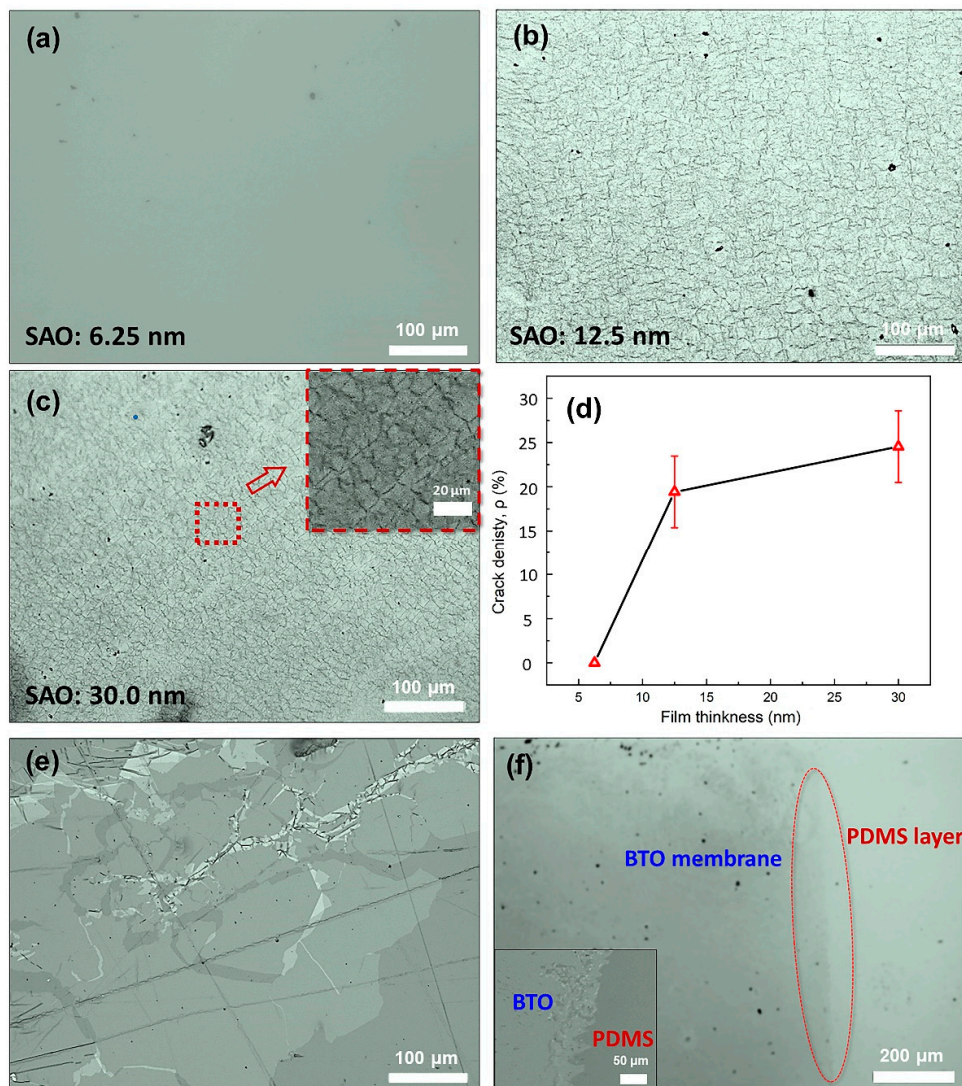


**Figure 3.** Optical micrographs of the 8.33-nm-thick BTO membranes separated from the SAO sacrificial layers with different thickness: (a) 6.25 nm; (b) 12.5 nm; (c) 30 nm. (d) Crack density for the BTO membranes as a function of the SAO thickness. (e) The freestanding BTO membranes separated from the deionized water directly. (f) Optical micrograph of the freestanding BTO membrane after the cross-section of the BTO/SAO/STO (001) structure was ground with fine sandpapers; the inset shows the cross-section structure was scraped with a blade.

During the deposition process of the BTO, the SAO sacrificial layer was completely covered by the BTO membrane and could not come in contact with the deionized water. Thus, the BTO membrane could not be separated from the growth substrate after the BTO/SAO/STO (001) structure was soaked for a week. To solve this problem, we scraped the cross-section of the BTO/SAO/STO (001) structure with a blade, making sure the SAO sacrificial layer was exposed to deionized water, and then the freestanding BTO membrane could be obtained successfully. In the morphology of the transferred BTO membrane, as shown in inset Figure 3f, a jagged edge structure appears in the BTO membrane scraped with a blade. The jagged edge structure increases the contact area between the SAO sacrificial layer and deionized water, which accelerates the dissolution rate, and the rapid stress change between the membrane and the substrate caused numerous cracks. To reduce the cracks in the edge area, we chose to use fine sandpapers (#1000) to grind the cross-section of the BTO/SAO/STO (001) structure slightly. Figure 3f shows the surface morphology of the treated structure, and the red dotted circle represents the edge of the membrane. The treated structure can be separated from the substrate after immersing

in deionized water for up to 48 h, and then the edge of the membrane was very flat and no cracks appeared. It is important to note that all the heterostructure edges were ground by fine sandpaper, in order to obtain high-quality freestanding membranes.

### 3.5. The Relationship between Crack Density and the Thickness for LSMO Layers

Considering that the BTO membrane directly contacts the PDMS during the transfer process, it is difficult to obtain an intact surface due to non-uniform surface forces. An LSMO cover layer was grown on the BTO membrane to form an LSMO/BTO heterostructure, so the LSMO layer directly contacts the PDMS instead of the BTO during transfer. Additionally, the LSMO layer can be used as an electrode for electrical performance measurements [32].

Anja et al. reported the evolution of the in-plane lattice constant of the  $\text{Pr}_{0.48}\text{Ca}_{0.52}\text{MnO}_3$  (PCMO) thin films ranging from 10 to 100 nm. For the 10-nm-thick sample, the  $a$  axes of film and substrate match perfectly, while the  $c$  axis is reduced compared to the bulk value. With increasing thickness, both the  $a$  and  $c$  axes of the PCMO film relax towards their bulk values, and the epitaxial strain may be relieved through the formation of cracks [33]. In the case of the LSMO (10 nm)/BTO (8.33 nm) heterostructure, the flat surface with cracks is clearly observed in Figure 4a. On the other hand, drastic change in the surface morphology above the LSMO (20 nm)/BTO (8.33 nm) and LSMO (30 nm)/BTO (8.33 nm) heterostructures were found, as shown in Figure 4b,c. The crack density increased systematically with increasing the LSMO layer thickness, as shown in Figure 4d. When the LSMO layer is grown epitaxially on the BTO membrane, in-plane tensile strain exists in the LSMO layer, caused by the lattice mismatch between the LSMO layer ( $\sim 3.85 \text{ \AA}$ ) and the SAO sacrificial layer ( $\sim 4.04 \text{ \AA}$ ). With increasing thickness of the LSMO layer, the lattice constant of the LSMO becomes smaller, leading to an increase in the epitaxial strain in the heterostructure. Then the epitaxial strain is clearly released by the formation of cracks.

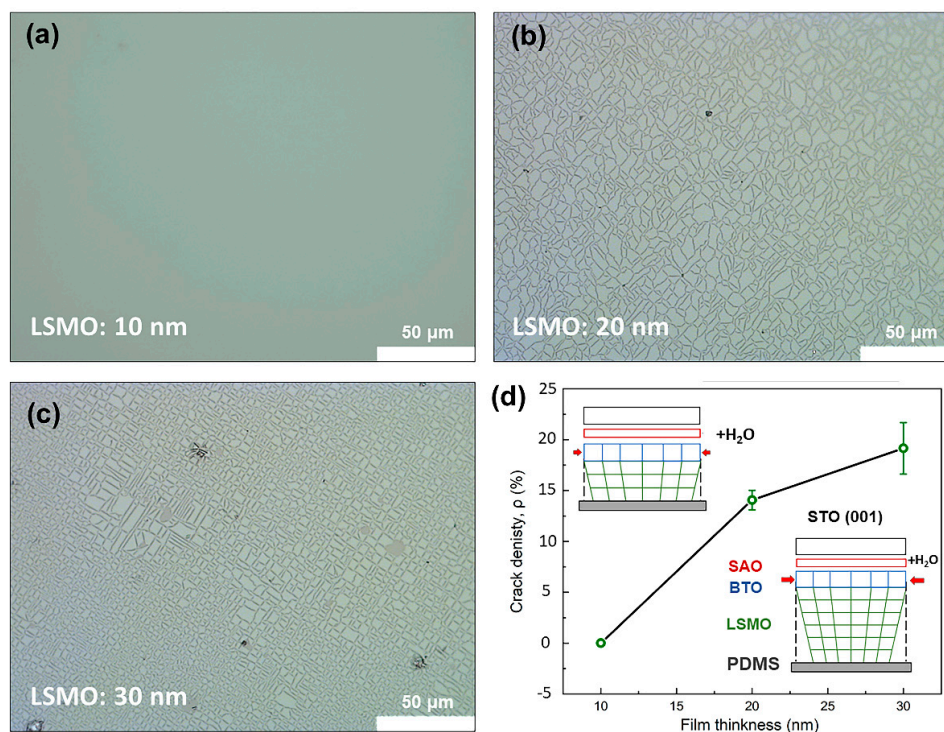


**Figure 4.** Serial optical micrographs of the BTO separated covered by different thickness of the LSMO layers: (a) 10 nm; (b) 20 nm; (c) 30 nm. (d) Changing in crack density for the LSMO/BTO (8.33 nm) membranes.

#### 4. Conclusions

To conclude, we systematically summarized the influence of the thickness of the SAO sacrificial layer and the BTO membrane on the crack density. By improving the transfer process, the BTO membrane with an area  $>700 \times 530 \mu\text{m}^2$  with no cracks can be obtained from the BTO (8.33 nm)/SAO (6.25 nm)/STO (001) substrate structure. Then, we improved the positive effect of the LSMO cover layer with the electrode function on crack elimination. After being separated from the substrate, a high-quality freestanding LSMO (10 nm)/BTO (8.33 nm) heterojunction can be obtained. On this basis, an unprecedented very large strain gradient can be generated by altering the radius of the freestanding single-crystal BTO membrane, the flexoelectric effects of which are yet to be explored.

**Author Contributions:** Conceptualization, W.L. and Q.W.; methodology, Q.W., H.F., B.H. and D.W.; software, Q.W.; validation, W.L. and Q.W.; formal analysis, W.L. and Q.W.; investigation, Q.W., J.W. and N.Z.; resources, W.L.; data curation, Q.W.; writing—original draft preparation, Q.W. and W.L.; writing—review and editing, W.L. and Q.W.; visualization, Q.W.; supervision, W.L.; project administration, W.L.; funding acquisition, W.L. All authors have read and agreed to the published version of the manuscript.

**Funding:** This work was supported by the National Natural Science Foundation of China (No. 51602080).

**Acknowledgments:** The authors appreciate the help with Python code writing from Jinhui Fan.

**Conflicts of Interest:** The authors declare no conflict of interest.

#### References

1. Paskiewicz, D.M.; Sichel-Tissot, R.; Karapetrova, E.; Stan, L.; Fong, D.D. Single-crystalline SrRuO<sub>3</sub> nanomembranes: A platform for flexible oxide electronics. *Nano Lett.* **2016**, *16*, 534–542. [[CrossRef](#)] [[PubMed](#)]
2. Won, S.S.; Seo, H.; Kawahara, M.; Glinsek, S.; Lee, J.; Kim, Y.; Jeong, C.K.; Kingon, A.I.; Kim, S.H. Flexible vibrational energy harvesting devices using strain-engineered perovskite piezoelectric thin films. *Nano Energy* **2019**, *55*, 182–192. [[CrossRef](#)]
3. Gao, W.; You, L.; Wang, Y.; Yuan, G.; Chu, Y.H.; Liu, Z.; Liu, J.M. Flexible PbZr<sub>0.52</sub>Ti<sub>0.48</sub>O<sub>3</sub> capacitors with giant piezoelectric response and dielectric Tunability. *Adv. Electron. Mater.* **2017**, *3*, 1600542. [[CrossRef](#)]
4. Kim, J.; De Araujo, W.R.; Samek, I.A.; Bandodkar, A.J.; Jia, W.; Brunetti, B.; Paixao, T.R.L.C.; Wang, J. Wearable temporary tattoo sensor for real-time trace metal monitoring in human sweat. *Electrochem. Commun.* **2015**, *51*, 41–45. [[CrossRef](#)]
5. Chen, M.; Li, Z.; Li, W.; Shan, C.; Li, W.; Li, K.; Gu, G.; Feng, Y.; Zhong, G.; Wei, L.; et al. Large-scale synthesis of single-crystalline self-standing SnSe<sub>2</sub> nanoplate arrays for wearable gas sensors. *Nanotechnology* **2018**, *29*, 455501. [[CrossRef](#)]
6. Li, J.; Liu, Y.; Zhang, Y.; Cai, H.L.; Xiong, R.G. Molecular ferroelectrics: Where electronics meet biology. *Phys. Chem. Chem. Phys.* **2013**, *15*, 20786–20796. [[CrossRef](#)]
7. You, Y.M.; Liao, W.Q.; Zhao, D.; Ye, H.Y.; Zhang, Y.; Zhou, Q.; Niu, X.; Wang, J.; Li, P.F.; Fu, D.W.; et al. An organic-inorganic perovskite ferroelectric with large piezoelectric response. *Science* **2017**, *357*, 306–309. [[CrossRef](#)]
8. Keimer, B. Transition metal oxides-ferroelectricity driven by orbital order. *Nat. Mater.* **2006**, *5*, 933–934. [[CrossRef](#)]
9. Yuasa, S.; Nagahama, T.; Fukushima, A.; Suzuki, Y.; Ando, K. Giant room-temperature magnetoresistance in single-crystal Fe/MgO/Fe magnetic tunnel junctions. *Nat. Mater.* **2004**, *3*, 868–871. [[CrossRef](#)]
10. He, S.; He, J.; Zhang, W.; Zhao, L.; Liu, D.; Liu, X.; Mou, D.; Ou, Y.B.; Wang, Q.Y.; Li, Z.; et al. Phase diagram and electronic indication of high-temperature superconductivity at 65 K in single-layer FeSe films. *Nat. Mater.* **2013**, *12*, 605–610. [[CrossRef](#)]
11. Mahmoud, A.E.; Afify, A.S.; Saed, E.M.; Gergs, M.K. Effect of processing conditions on (Ba<sub>1-x</sub>Ca<sub>x</sub>)(Ti<sub>0.9</sub>Sn<sub>0.1</sub>)O<sub>3</sub> lead-free ceramics for the enhancement of structural, humidity sensing and dielectric properties. *J. Aust. Ceram. Soc.* **2019**, *55*, 933–942. [[CrossRef](#)]
12. Mahmoud, A.E.; Afify, A.S.; Mohamed, A. The crossover of (Ba<sub>1-x</sub>Ca<sub>x</sub>)(Ti<sub>0.9</sub>Sn<sub>0.1</sub>)O<sub>3</sub> piezoelectric ceramics from single-phase to composite with studying the structural and dielectric properties. *J. Mater. Sci. Mater. Electron.* **2017**, *28*, 11591–11602. [[CrossRef](#)]

13. Luo, Z.D.; Peters, J.J.P.; Sanchez, A.M.; Alexe, M. Flexible memristors based on single-Crystalline ferroelectric tunnel junctions. *ACS Appl. Mater. Interfaces* **2019**, *11*, 23313–23319. [[CrossRef](#)] [[PubMed](#)]
14. Qin, Q.H.; Akaslopolo, L.; Tuomisto, N.; Yao, L.; Majumdar, S.; Vijayakumar, J.; Casiraghi, A.; Inkinen, S.; Chen, B.; Zugarramurdi, A.; et al. Resistive switching in all-oxide ferroelectric tunnel junctions with ionic interfaces. *Sci. Adv.* **2016**, *28*, 6852–6859. [[CrossRef](#)]
15. Yau, H.M.; Xi, Z.; Chen, X.; Wen, Z.; Wu, G.; Dai, J.Y. Dynamic strain-induced giant electroresistance and erasing effect in ultrathin ferroelectric tunnel-junction memory. *Phys. Rev. B* **2017**, *95*. [[CrossRef](#)]
16. Wen, Z.; Qiu, X.; Li, C.; Zheng, C.; Ge, X.; Li, A.; Wu, D. Mechanical switching of ferroelectric polarization in ultrathin BaTiO<sub>3</sub> films: The effects of epitaxial strain. *Appl. Phys. Lett.* **2014**, *104*, 042907. [[CrossRef](#)]
17. Lu, W.; Li, C.; Zheng, L.; Xiao, J.; Lin, W.; Li, Q.; Wang, X.R.; Huang, Z.; Zeng, S.; Han, K.; et al. Multi-nonvolatile state resistive switching arising from ferroelectricity and oxygen vacancy migration. *Adv. Mater.* **2017**, *29*, 1606165. [[CrossRef](#)]
18. Sun, Z.; Li, J.; Ji, C.; Sun, J.; Hong, M.; Luo, J. Unusual long-range ordering incommensurate structural modulations in an organic molecular ferroelectric. *J. Am. Chem. Soc.* **2017**, *139*, 15900–15906. [[CrossRef](#)]
19. Jiang, J.; Bitla, Y.; Huang, C.W.; Do, T.H.; Liu, H.J.; Hsieh, Y.H.; Ma, C.H.; Jang, C.Y.; Lai, Y.H.; Chiu, P.W.; et al. Flexible ferroelectric element based on van der Waals heteroepitaxy. *Sci. Adv.* **2017**, *3*. [[CrossRef](#)]
20. Dong, G.; Li, S.; Yao, M.; Zhou, Z.; Zhang, Y.Q.; Han, X.; Luo, Z.; Yao, J.; Peng, B.; Hu, Z.; et al. Super-elastic ferroelectric single-crystal membrane with continuous electric dipole rotation. *Science* **2019**, *366*, 475–479. [[CrossRef](#)]
21. Lu, D.; Baek, D.J.; Hong, S.S.; Kourkoutis, L.F.; Hikita, Y.; Hwang, H.Y. Synthesis of freestanding single-crystal perovskite films and heterostructures by etching of sacrificial water-soluble layers. *Nat. Mater.* **2016**, *15*, 1255–1260. [[CrossRef](#)] [[PubMed](#)]
22. Chen, Z.; Wang, B.Y.; Goodge, B.H.; Lu, D.; Hong, S.S.; Li, D.; Kourkoutis, L.F.; Hikita, Y.; Hwang, H.Y. Freestanding crystalline YBa<sub>2</sub>Cu<sub>3</sub>O<sub>7-x</sub> heterostructure membranes. *Phys. Rev. Mater.* **2019**, *3*. [[CrossRef](#)]
23. Ji, D.; Cai, S.; Paudel, T.R.; Sun, H.; Zhang, C.; Han, L.; Wei, Y.; Zang, Y.; Gu, M.; Zhang, Y.; et al. Freestanding crystalline oxide perovskites down to the monolayer limit. *Nature* **2019**, *570*, 87–90. [[CrossRef](#)] [[PubMed](#)]
24. Han, K.; Hu, K.; Li, X.; Huang, K.; Huang, Z.; Zeng, S.; Qi, D.; Ye, C.; Yang, J.; Xu, H.; et al. Erasable and recreatable two-dimensional electron gas at the heterointerface of SrTiO<sub>3</sub> and a water-dissolvable overlayer. *Sci. Adv.* **2019**, *5*. [[CrossRef](#)] [[PubMed](#)]
25. Zhu, X.; Zhang, B.; Gao, J.; Zhang, G. Evaluation of the crack-initiation strain of a Cu–Ni multilayer on a flexible substrate. *Scr. Mater.* **2009**, *60*, 178–181. [[CrossRef](#)]
26. Niu, R.M.; Liu, G.; Wang, C.; Zhang, G.; Ding, X.D.; Sun, J. Thickness dependent critical strain in submicron Cu films adherent to polymer substrate. *Appl. Phys. Lett.* **2007**, *90*, 161907. [[CrossRef](#)]
27. Canedy, C.L.; Li, H.; Alpay, S.P.; Salamanca-Riba, L.; Roytburd, A.L.; Ramesh, R. Dielectric properties in heteroepitaxial Ba<sub>0.6</sub>Sr<sub>0.4</sub>TiO<sub>3</sub> thin films: Effect of internal stresses and dislocation-type defects. *Appl. Phys. Lett.* **2000**, *77*, 1695–1697. [[CrossRef](#)]
28. Sinnamon, L.J.; Bowman, R.M.; Gregg, J.M. Thickness-induced stabilization of ferroelectricity in SrRuO<sub>3</sub>/Ba<sub>0.5</sub>Sr<sub>0.5</sub>TiO<sub>3</sub>/Au thin film capacitors. *Appl. Phys. Lett.* **2002**, *81*, 889–891. [[CrossRef](#)]
29. Won, S.; Jung, H.J.; Kim, D.; Lee, S.H.; Lam, D.V.; Kim, H.D.; Kim, K.S.; Lee, S.M.; Seo, M.; Kim, D.S.; et al. Graphene-based crack lithography for high-throughput fabrication of terahertz metamaterials. *Carbon* **2020**, *158*, 505–512. [[CrossRef](#)]
30. Deng, S.; Berry, V. Wrinkled, rippled and crumpled graphene: An overview of formation mechanism, electronic properties, and applications. *Mater. Today* **2016**, *19*, 197–212. [[CrossRef](#)]
31. Han, S.T.; Zhou, Y.; Roy, V.A.L. Towards the development of flexible non-volatile memories. *Adv. Mater.* **2013**, *25*, 5425–5449. [[CrossRef](#)] [[PubMed](#)]
32. Wu, W.B.; Wong, K.H.; Choy, C.L.; Zhang, Y.H. Top-interface-controlled fatigue of epitaxial Pb(Zr<sub>0.52</sub>Ti<sub>0.48</sub>)O<sub>3</sub> ferroelectric thin films on La<sub>0.7</sub>Sr<sub>0.3</sub>MnO<sub>3</sub> electrodes. *Appl. Phys. Lett.* **2000**, *77*, 3441–3443. [[CrossRef](#)]
33. Anja, H.; Kerry, J.O.; Donald, A.M.; Michael, N.; Berand, R.; Ulrich, S.; Regina, D. Competing strain relaxation mechanisms in epitaxially grown Pr<sub>0.48</sub>Ca<sub>0.52</sub>MnO<sub>3</sub> on SrTiO<sub>3</sub>. *APL Mater.* **2014**, *2*, 106106.

